Measurement of the $^2H(p, 2p)n$ Reaction over a Large Volume of Phase Space*

J. G. Rogers, Mahavir Jain, and J. D. Bronson
Cyclotron Institute, Texas A & M University, College Station, Texas 77843
(Received 26 March 1973)

A kinematically complete measurement of the deuteron breakup cross section has been made using a 39.5-MeV proton beam. The cross section was simultaneously measured at approximately 2000 angle pairs chosen to uniformly sample the entire phase-space volume available to the two protons. A portion of the data in the form of a partial Dalitz plot is compared with a simple model calculation. In the model, the breakup cross section is expressed as an incoherent sum of terms to separately represent the dependence of the cross section on statistical processes, pp quasifree scattering, and nucleon-nucleon final-state interactions. The model calculation does not reproduce the minimum in the partial Dalitz plot, consistent with the previously published hypothesis that the minimum is due to a destructive interference effect. The results of the model calculation are also compared with spectra at a representative set of individual angle pairs.

I. INTRODUCTION

Many three-body breakup experiments have been performed within the last decade. However, with the exception of high-energy bubble-chamber or photographic-emulsion experiments, these measurements have been made using two or at most a few detectors in coincidence. Thus, only particular types of nucleon + deuteron → 3 nucleons events have been investigated in any great detail, such as quasifree scattering (QFS) and final-state interactions (FSI). The limited scope of these experiments generally has permitted satisfactory fits to the data by theoretical calculations utilizing simple approximations valid only in the limited region investigated.

The present experiment was performed to overcome these limitations by providing data for $^2H(p, 2p)n$ reaction in 4π geometry.[1] In this article, the details of the experimental technique used to obtain such a general set of data and the comparison of the data with a simple model over a large region of phase space will be reported. A comparison of the data with an exact calculation based on a separable potential model will appear in another article.[2]

II. APPARATUS AND EXPERIMENTAL TECHNIQUE

To provide such a general set of data, the following conditions were imposed. First, two of the three final-state particles were detected in coincidence. Second, the energies and directions of emission of the two detected particles were determined. This provided six parameters for each event whereas only five are needed in principle to completely determine the final-state kinematics. However, the additional information is necessary to resolve double-valued kinematic solutions, to enable the elimination of unwanted background events, and to provide a check on the reliability of the detection apparatus. Third, all directions of emission of the two detected particles were uniformly sampled.

The apparatus has been described elsewhere in detail,[3] therefore only a brief summary will be given here. The scattering chamber consisted of two aluminum hemispheres, each of radius 61 cm and nominal wall thickness of 2.5 cm. The detector system contained 192 scintillation detectors divided into two data channels of 96 detectors each. The two detector systems differed only in the arrangement of the detector locations on the surface of the sphere. If the two detected particles and the undetected particles are labeled as 3, 4, and 5, respectively, the system for detecting particle 3 was arranged uniformly in $\cos\theta_3$ and ϕ_3. The second system was also arranged uniformly in $\cos\theta_4$. Since the three-body cross section does not vary independently with ϕ_3 and ϕ_4, but depends on $\Delta\phi$ $(=\phi_3 - \phi_4)$, it was only necessary to arrange the second system to uniformly sample the azimuthal-angle difference $\Delta\phi$. The second system is concentrated in a narrow region of ϕ_4 space, which increases the density of the sampling points in the $\Delta\phi$ variable. The system for detecting particle 3 is called the "coarse" system since it is distributed over the entire 2π in ϕ_3, whereas the system for detecting particle 4 is called the "fine" system since it is effectively distributed over only $\frac{1}{8}$ of the 2π range of ϕ_4. The apparatus described samples the three-dimensional $\cos\theta_3 \cos\theta_4 \Delta\phi$ volume at 9216 $(=96^2)$ equally spaced points; however, the $^2H(p, 2p)n$ three-body kinematics restrict the valid events to about 2000 of the possible 9216 pairs of detectors.

Each scintillation detector consisted of a cylinder of NE102 (2.85-cm diameter × 5.1-cm length) cemented onto the face of an RCA-4517 photomulti-

plier tube. The average solid angle subtended by the detectors was 2.3 msr. The front face of the scintillator was polished and the sides coated with reflecting paint. Charged particles were prevented from entering the scintillators through the sides by 0.3-cm-thick brass sleeves. The electronics attached individually to each photomultiplier consisted of a standard voltage divider chain and capacitively coupled outputs to provide the number of signals required by the data channel. Linear and fast-timing signals were taken from the 7th and 10th dynodes, respectively. The anode output was divided into three signals to be used in the detector identification–coding network. All outputs except the linear one were diode isolated to prevent cross talk between detectors and between coding lines.

Figure 1 shows a simplified block diagram of the electronics. The information presented by each of the two data channels consisted of a fast signal for timing and a linear signal for pulse height or energy information, and a set of coding signals to identify the specific detector involved. The 96 linear and 96 fast signals from each channel are fanned in resistively and fed to a fast amplifier and timing discriminator, respectively. The 16 coding signals from each channel feed 16 low-level discriminators with variable electronic delays, the only nonstandard modules used in the system.

A complete coincidence event consisted of five parameters: two linear signals, two sets of coding signals, and a relative time-of-flight (TOF) signal. Whenever a particle was detected in one of the detectors of the coarse system within 250 nsec of a particle detected in one of the detectors of the fine system, the five parameters were converted to digital form by analog-to-digital converters (ADC's) and DCB's[4] and recorded by a modified IBM-7094 computer. The computer checked the two coding words to reject triple coincidence events which composed about 3% of the incoming data. The five parameters from the valid events were recorded on magnetic tape. A pulse-height spectrum from each of the 192 detectors as well

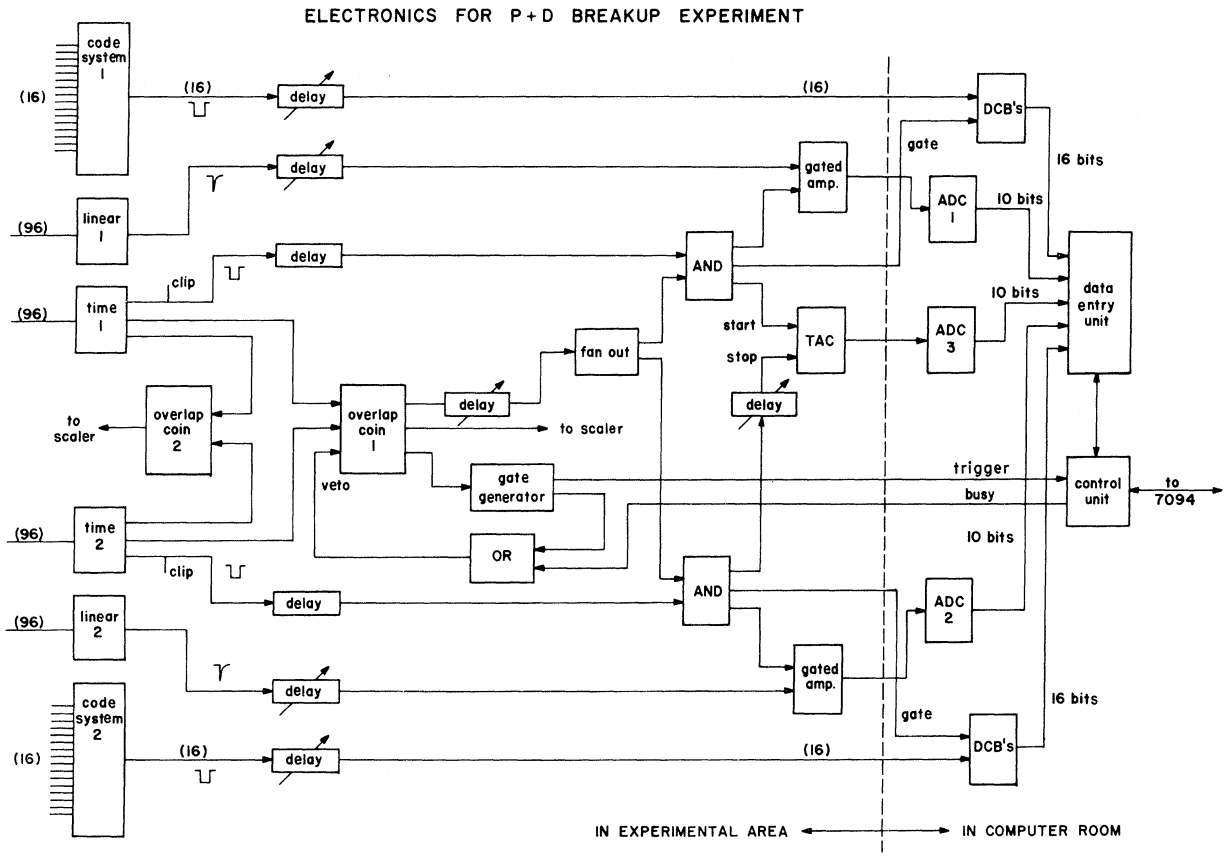

FIG. 1. A block diagram of the electronics used in the $^2H(p,2p)n$ experiment. All modules are standard NIM electronics except for the 16-channel "code-system" discriminators. TAC is time-to-amplitude converter; DCB is discriminator-coincidence-buffer register.

as the TOF spectrum were also stored in the computer. The stored spectra could be displayed or printed during acquisition.

The 39.5-MeV proton beam from the cyclotron was carefully collimated and aligned with scintillating phosphors to guarantee that it passed through the chamber on the axis of the detector system. The uncertainty in the polar angle of the detectors was at worst ±0.5°, but most of the detectors were within 0.3° of their nominal positions. The principal target was a deuterated polyethylene foil of thickness[5] 0.5–0.8 mg/cm^2. The beam spot on the target was approximately a circle of diameter 0.6 cm.

To avoid the shadowing of certain detectors by the target frame and distortion of the measured spectra due to the energy loss of the emerging protons in the target, data were acquired for different orientations of the target foil so that the proton momenta always made an angle greater than 15° with the target plane. This limiting angle corresponds to a worst-case average energy spread of ±0.12 MeV at a proton energy of 5 MeV.

Beam currents of 0.3–0.6 nA were used, which produced a coincidence counting rate of 50–100 events/sec. During each coincidence run a spectrum was measured by an independent monitor detector at $\theta_{lab} = 45°$. The C(p, p)C elastic peak in the monitor spectrum was integrated to determine the target-beam normalization for each run using the known elastic cross section[6] and C/D ratio of the CD_2 foil. About 6.5 million coincidence events were recorded from CD_2.

In addition to the coincidence runs with a CD_2 target, singles spectra were recorded in each of the 192 detectors under conditions identical to the coincidence runs, using CH_2, CD_2, and carbon foils. These spectra were used for calibrating the gain of each detector in off-line processing.

Coincidence runs were also made with CH_2 and carbon foils. The CH_2 data were to allow subtraction of a background from the 1% residual hydrogen contained in the deuterated foil. Because of the small kinematic difference between elastic and quasifree pp scattering, we were unable to resolve these two events kinematically in the few pairs of detectors which had $\theta_3 + \theta_4 \approx 90°$, $\Delta\phi \approx 180°$. The carbon data were subtracted from the CD_2 data to correct for small backgrounds of real events from C$(p, 2p)$, C$(p, p\alpha)$, etc.

III. DATA REDUCTION

Before comparisons could conveniently be made with model predictions, the data were further processed by the computer. The first step in the processing was to convert each pulse height into a proton energy. It is well known that the light produced by protons in the NE102 scintillator is a nonlinear function of the proton energy. We determined the average response function for several of the detectors by adjusting the constants kB and C in the expression from Ref. 7 for the total light (L) produced in NE102 by a proton which looses all of its energy (E_p) in the scintillator:

$$L(E_p) = \int_0^{E_p} \left[1 + kB\left(\frac{dE}{dx}\right) + C\left(\frac{dE}{dx}\right)^2\right]^{-1} dE \,. \tag{1}$$

Since the departure from linearity is largest at low energies, we used the low-energy protons from elastic hydrogen scattering at large angles to determine the parameters kB and C in Eq. (1). Figure 2 shows one of the CH_2 singles spectra used for this purpose. After determining the best average response function for the selected group of detectors, it was found that for the entire group of detectors the light output given by Eq. (1) was not a linear function of pulse height or channel number. To compensate for this additional nonlinearity we used a quadratic relationship between the light and the recorded channel number:

$$L(E_p) = g_1 N + g_2 N^2 \,, \tag{2}$$

where g_1 and g_2 are the gain constants for each detector which relate the channel number (N) to the energy (E_p) via the function in Eq. (1). The gain constants g_1 and g_2 were determined independently for each of the 192 detectors by using the known energies of the protons scattered from carbon and

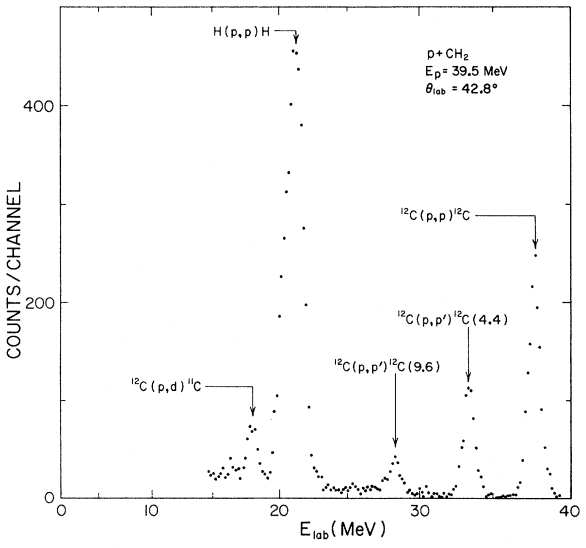

FIG. 2. A singles spectrum from a CH_2 target for a typical one of the 192 detectors. The arrows indicate the positions of the peaks used to determine the NE102 response function and detector-gain constants.

CH_2. The median positions of the peaks corresponding to scattering from the ground and 9.6-MeV excited state of carbon were found by a search program and used to determine g_1 and g_2 by solving the simultaneous equations resulting from Eq. (2) above. Figure 2 shows a typical calibration spectrum. The over-all response function $E_p(N)$ from combining Eqs. (1) and (2) was displayed by the program after calibrating the spectrum from each detector. The expected positions of the other peaks in each calibration spectrum were indicated by markers on the displayed spectrum. A light pen was used to interrupt and correct the computer calibration in cases where statistical variations in the spectra caused the automatic peak search to fail. The stability of the detector gains with time was checked by independently determining a complete set of g_1 and g_2 from calibration data acquired at the beginning, in the middle, and at the end of the set of coincidence runs. It was found that for all but 13 of the detectors, the gains were constant to within 5%. For the detectors which showed gain shifts during acquisition, g_1 and g_2 were changed as a function of time in analyzing the coincidence data sets.

After the gain constants were determined for all detectors, the raw-data tapes were processed to form an intermediate set of tapes which also contained a list of parameters describing each event in order. These parameters were the two laboratory energies of the protons, the two detector locations, and a corrected-relative-time parameter. The corrected time was computed from the recorded TOF parameter by subtracting the time differences in the protons' arrival times due to the actual times of flight from the target to detector and due to the differences in the cable lengths connecting the detectors to the electronics. The resulting peaks for the real and accidental coincidence events had a width mainly due to transit-time differences in the photomultiplier tubes, discriminator walk, and to some extent due to resolution effects. A typical time spectrum is shown before and after correction in Fig. 3. The accidental coincidence events were less than 10% of the real coincidence data except in the detectors at the smallest θ angles where the real and accidental rates were at worst about equal. The accidental coincidence events were largely due to elastic scattering from carbon and deuterium and were therefore kinematically separate from the valid $^2H(p, 2p)n$ events.

The intermediate data tapes were read by the computer to form the data contained in the time-zero (real coincidence) peak of the relative-time spectrum into about 2000 arrays of counts as a function of the two proton energies, E_3 and E_4; an array was formed for each pair of detectors which was kinematically allowed to detect $^2H(p, 2p)n$ events. The accidental events in the peak one rf period later in the corrected-time spectrum for each pair were subtracted from the time-zero events in the E_3-E_4 arrays. In addition, E_3-E_4 arrays were formed from the carbon data, normalized to the CD_2 data using the monitor-detector data, and subtracted.

The final $^2H(p, 2p)n$ data from all the coincidence runs exist as a list of 2000 two-dimensional energy spectra on one reel of magnetic tape. To form projected cross sections $(d^5\sigma/d\Omega_3 d\Omega_4 dE)$ the tape was read and the E_3-E_4 data projected on the E_3 and E_4 axes with the appropriate normalization factor as determined by the elastic carbon monitor for all the runs included in the spectrum. Such an E_3-E_4 plot and projected spectra are shown for a particular pair of angles in Fig. 4. The sources of the various background events in Fig. 4 are discussed in Sec. IV of this article.

The uncertainty in the absolute cross-section normalization for the entire data set includes con-

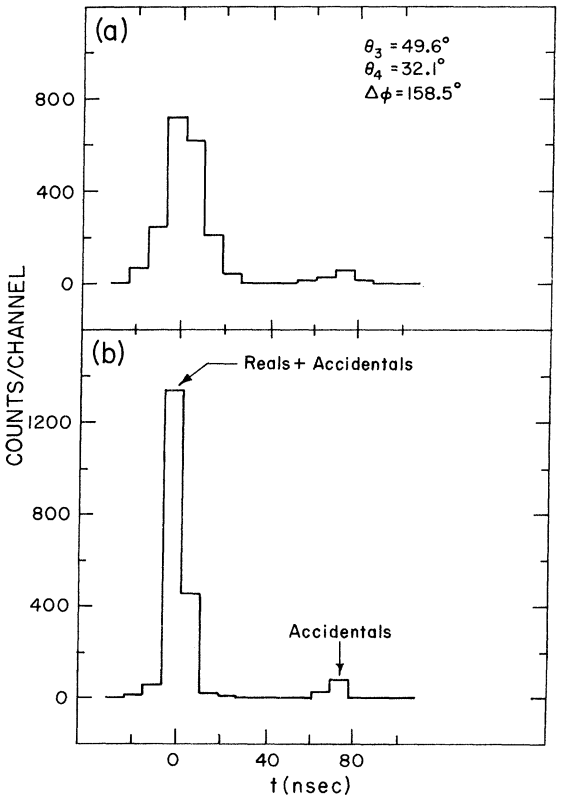

FIG. 3. A relative-time spectrum for a particular pair of detectors from the time-to-amplitude converter. (a) The raw spectrum including cable delays and particle times-of-flight. (b) The same spectrum after correction for cable delays and times-of-flight.

tributions from the statistical uncertainty of the total monitor count (0.6%), uncertainty in the 45° carbon elastic cross section[8] (4%), uncertainty in the monitor solid angle (1%), uncertainty in the monitor dead time (1%), and uncertainty in the C/D ratio of deuterated polyethylene (1%). To verify that the C/D ratio was constant, we simultaneously measured the scattering from the carbon and deuterium in the CD_2 throughout the course of the data taking. The ratio was constant to within 1%. In addition to the uncertainty in over-all normalization, there was a relative uncertainty from spectrum to spectrum due to uncertainties in the detector solid angles (3%) and the relative statistical uncertainty in the monitor counts for different runs (1%). We estimate the uncertainty in the absolute cross sections from these sources to be ±6%, to which must be added the statistical uncertainty of the $^2H(p,2p)n$ counts as indicated by the error bars on the spectra discussed in this article.

In addition to the uncertainties mentioned above, the detection of $^2H(p,pn)p$ events produced a background in the region of the three-body kinematic loci. The only reliable measure we have of this

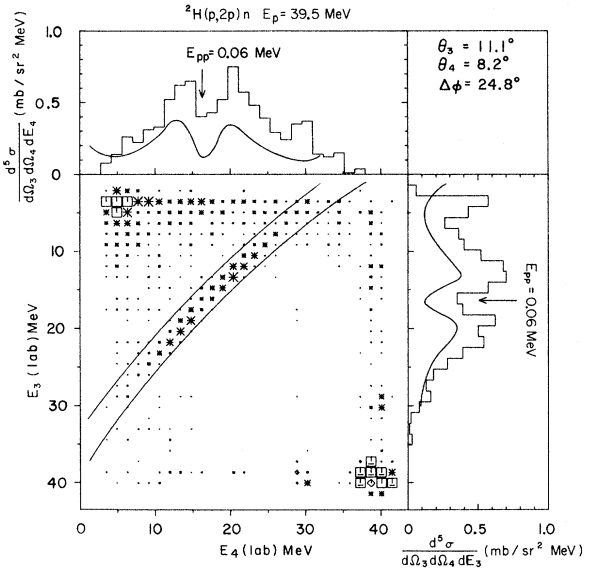

FIG. 4. An E_3-E_4 plot of counts vs laboratory proton energies. Each asterisk in the two-dimensional portion is of a linear size proportional to the counts in that E_3-E_4 channel. The curved lines in the two-dimensional energy spectrum enclose the band which can contain valid $^2H(p,2p)n$ events. The two histograms are the projection of the data between these lines onto the E_3 and E_4 axes with scaling appropriate to converting the counts to cross section. The solid curves in the projected spectra are the prediction of the model discussed in Sec. IV of this article.

background is in the nucleon-nucleon quasifree-scattering region of phase space where both the $^2H(p,2p)n$ and $^2H(p,pn)p$ cross sections have been measured.[9] In this region we determined the $^2H(p,pn)p$ background to be about 5% of the data in the projected spectra. Because the $^2H(p,pn)p$ cross section in the pn-QFS region is about 2.5 times larger[9] than the $^2H(p,2p)n$ cross section in the pp-QFS region, this 5% figure is probably the worst-case contribution from this source of background. In regions away from pp-QFS this background should be usually less than 2% since in these regions the $^2H(p,pn)p$ cross section will on the average be less than the $^2H(p,2p)n$ cross section. The integrated $^2H(p,2p)n$ cross section must equal the integrated $^2H(p,pn)p$ cross section. The $^2H(p,pn)p$ background has not been subtracted from the data presented in this article.

IV. ANALYSIS OF THE DATA

A. Partial Dalitz Plot Data

Because we have measured about 2000 kinematically complete spectra, it was impractical to follow the usual procedure of calculating a model prediction for comparison with each individual spectrum. The model we will discuss in this article is one which contains a small number of adjustable parameters to be fitted to the data.[10] To extract an average set of fitting parameters, we utilized the three-body data in the form of a partial Dalitz plot, shown in Fig. 5. As described in Ref. 11, the partial Dalitz plot was formed by integrating the data over the possible angles of emission of one of the protons. For fixed θ_4, ϕ_4 the cross section of the partial Dalitz plot is given by[12,13]

$$\frac{d^4\sigma}{d\Omega_4 dE_3 dE_4}(E_3,E_4)=\int d\Omega_3 \frac{d^6\sigma}{d\Omega_3 d\Omega_4 dE_3 dE_4}\delta(\theta_3'-\theta_3)\,, \tag{3}$$

where the δ function is explicitly included to guarantee that the contribution to the integral is zero for points off the three-body locus. Using the data we have acquired, we can approximate the exact expression given by Eq. (3) by adding up the E_3-E_4 data from selected detector pairs with appropriate normalizations. We selected detectors at fixed θ_4 from the "fine" detector system so that the uniform coverage in the ϕ_3 direction by the "coarse" system could be utilized in approximating the integral. Both detector systems have uniform coverage in the $\cos\theta$ direction, so the integral was approximated by

$$\frac{d^4\sigma}{d\Omega_4 dE_3 dE_4}\approx\sum_i e_i B_i N_i(E_3,E_4) f_i(E_3,E_4)\,, \tag{4}$$

where the sum is over all detectors in the "coarse" system in coincidence with a detector at $\theta_4 \approx 43°$ in the "fine" system. N_i is the number of particles detected at energies E_3 and E_4 in the ith detector pair. B_i is the beam and target normalization for the ith pair and also contains the channel size $(1/\Delta\Omega_4 \Delta E_3 \Delta E_4)$ to give the cross section the proper dimensions of μb/sr MeV^2. The coverage coefficient $e_i(\approx 58)$ [14] is included to express the fact that each of the "coarse" system detectors samples only a fraction $(1/\Delta\Omega_i)$ of the 4π solid angle available to particle 3. The function f_i is an approximation to the δ function in Eq. (3). The explicit inclusion of the δ function in the approximation of the integrated cross section would not be necessary in an ideal experiment since the measured cross section would naturally be zero off the kinematic locus, but including the δ function is an essential means of reducing the background in an actual experiment. To illustrate the importance of this technique in the present experiment, we show a worst-case E_3-E_4 spectrum in Fig. 4. With no finite-resolution effects, the counts from ^{2}H-$(p, 2p)n$ would lie on a line between the solid lines drawn on the two-dimensional plot. Because of resolution effects in angle and energy, the actual data lie on a band of finite width. The curved lines are loci generated by assuming a difference in the total center-of-mass kinetic energy of +14% and −11% from the actual energy. Events between the lines were taken as acceptable ^{2}H$(p, 2p)n$ events while events outside the lines were considered background events. The function f_i was taken to be unity inside the lines and zero outside the lines.

Figure 4 shows the data at the farthest forward angles in each system and contains some uniquely troublesome background events. The counts off the three-body locus at low values of E_3 and E_4 are mostly due to elastically scattered protons which suffer a nuclear collision in one of the detectors, producing uncharged products which were then detected in the second detector. These invalid events are only significant in detectors which are geometrically close together $(\theta_3 \approx \theta_4, \Delta\phi \approx 0)$. The unsubtracted bands of accidental coincidence events at $E_3 \approx 40$ MeV and $E_4 \approx 40$ MeV are also present predominantly only at the forward angles because the elastic cross sections of carbon and deuterium are large at small angles. To increase the sampling density in the $\Delta\phi$ direction, we averaged the cross section computed from Eq. (4) over four detectors in the "fine" system with equally spaced azimuthal angles and slightly different polar angles $(\theta_4 = 39, 43, 44, \text{and } 45°)$.

Data from 180 pairs of detectors were summed according to the prescription of Eq. (4). The range of θ_4 averaged over causes some smearing of the features in the data, but we will compare the Dalitz plot data with a model simulation averaged in a manner identical to that used for the data, so the simulation will be subject to the same distortion from this source as the data.

B. Model Simulation

To simulate the Dalitz plot cross section we made the following replacement in Eq. (4):

$$N_i(E_3, E_4) f_i(E_3, E_4) = \frac{1}{b_i} \left(\frac{d^5\sigma}{d\Omega_3 d\Omega_4 dE_3} \right)_i \delta(E_4' - E_4), \quad (5)$$

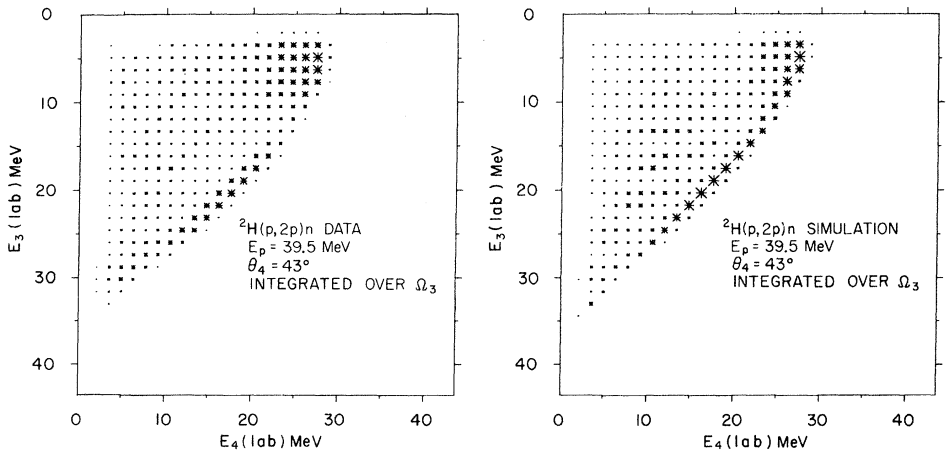

FIG. 5. A partial Dalitz plot of the ^{2}H$(p, 2p)n$ cross section at $\theta_4 \approx 43°$. Data from 180 detector pairs were integrated over Ω_3 for approximately constant θ_4. The linear size of each asterisk is proportional to $d^4\sigma/d\Omega_4 dE_3 dE_4$ at the indicated proton laboratory energies. The plot on the left is the measured ^{2}H$(p, 2p)n$ data. The plot on the right is a simulation of the data based on the model discussed in Sec. IV of this article. The largest asterisk represents a cross section of 191 μb/sr MeV^2.

where $(d^5\sigma/d\Omega_3 d\Omega_4 dE_3)_i$ is a model expression for the differential cross section which will be discussed below and b_i is the target-beam normalization analagous to B_i in Eq. (4). The energy δ function makes the contribution to the integral zero at $E_3 - E_4$ points off the kinematic locus for the ith detector pair. Notice that the rather broad function, $f_i(E_3, E_4)$, in Eq. (4) was replaced by a δ function in the simulation so we have not explicitly simulated the finite resolution effects discussed above.

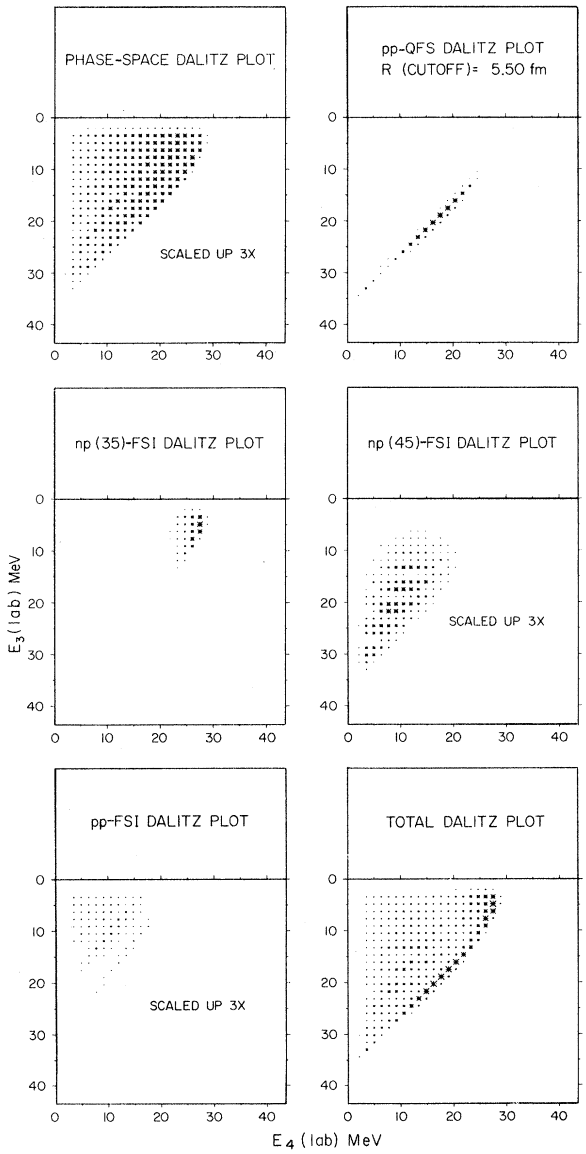

FIG. 6. Partial Dalitz plots of the contributions to the cross section by the individual terms of the model expression Eq. (6). The scale for three of the plots is the same as in Fig. 5 while the symbols in the plots labeled "scaled up 3X" have been enlarged by a factor of 3.

We took as our model expression for the cross section[10]

$$d^5\sigma/d\Omega_3 d\Omega_4 dE = \rho(A + F_{\text{msia}} + BF_{np} + CF_{pp}), \quad (6)$$

where ρ is the three-body phase-space function,[15] F_{msia} is the modified-simple-impulse approximation[16,17] term to represent pp quasifree scattering (QFS), and F_{np} and F_{pp} are Watson-Migdal[18] type enhancement factors to represent np[19] and pp[20] final-state interactions (FSI), respectively. A fit to the Dalitz plot data was made by independently adjusting the constants A, B, and C as well as the cutoff radius which occurs in F_{msia}. The contributions to the Dalitz plot by the various terms of Eq. (6) are shown in Fig. 6 and discussed below.

C. Phase-Space Term

The first term in Eq. (6) is proportional to the phase-space volume[15] available to the three particles. It is intended to represent the probability that the reaction proceeds through a statistical process which does not depend on the dynamics of the reaction. The phase-space factor (ρ) includes the s-wave Coulomb penetration factor[21] $C^2(\eta)$ to roughly account for the final-state repulsion of the two protons. This factor makes the model prediction for $d^5\sigma/d\Omega_3 d\Omega_4 dE$ zero at $E_{pp} = 0$, but has little effect on the cross section above $E_{pp} = 1$ MeV. The rapid variations from point to point in the phase-space Dalitz plot shown in Fig. 6 are indications that the representation of the integral by a finite sum over detector pairs is not entirely accurate. Except for a small Coulomb effect the phase-space Dalitz plot should be uniform in the E_3 direction for each E_4 and should show a smooth variation in the E_4 direction. The nonuniformities in the phase-space Dalitz plot are due to imperfect sampling by the "coarse" system of detectors but this does not detract from the comparison of the simulation with the data since the sum over the detector locations in Eq. (4) is the same for both.

D. Quasifree-Scattering Term

The second term in Eq. (6) contributes to the Dalitz plot in the region where the spectator-neutron energy $(= E_1 + Q - E_3 - E_4)$[22] is small, as shown in the pp-QFS plot of Fig. 6. The term F_{msia} used to represent pp-QFS is the version of the modified-simple-impulse approximation[16,17] which contains a sharp radial cutoff in the deuteron wave function to phenomenologically simulate the effects of rescattering in the impulse approximation. F_{msia} has the form:

$$F_{\text{msia}} = \frac{d\sigma}{d\Omega} |\phi_d(p_5)|^2, \quad (7)$$

where $d\sigma/d\Omega$ is the pp differential cross section and $\phi_d(p_5)$ is the momentum wave function of the deuteron, which contains the cutoff radius as a parameter. The best fit to the data was obtained with a radial cutoff of 5.5 fm in the deuteron's spatial wave function $\psi_d(r)$, which was Fourier transformed to obtain $\phi_d(p_5)$. Because of the sharp cutoff in $\psi_d(r)$, $\phi_d(p_5)$ is an oscillating function of the spectator-neutron momentum (p_5) with its first zero at $p_5 = 75$ MeV/c. It is unlikely that there is any physical significance to the oscillating behavior of $\phi_d(p_5)$ for large p_5, so only the first maximum of the oscillating function was retained in fitting the data. That is, we arbitrarily set $\phi_d(p_5) = 0$ for all p_5 greater than 75 MeV/c.

The usual choice for $d\sigma/d\Omega$ in Eq. (7) is the elastic pp cross section evaluated at the energy and scattering angle in the c.m. of the two final-state protons. The different possible choices of how to evaluate $d\sigma/d\Omega$ [23] produce nearly the same results when the modified-simple-impulse approximation is compared with ^{2}H(p, $2p$)n spectra near $p_5 = 0$ since the pp c.m. energy is in that case about the same in the initial state as in the final state (differing only by the Q value). However, in this calculation F_{msia} will contribute to the cross section up to rather large values of p_5, where the initial- and final-state pp relative energies are quite different. In this circumstance, it seems unreasonable to arbitrarily select the final-state relative energy as being more important than the initial-state relative energy in determining $d\sigma/d\Omega$. We have evaluated $d\sigma/d\Omega$ at an energy which is the *average* between the initial- and final-state pp c.m. energy.

A second problem which arises in evaluating $d\sigma/d\Omega$ for large p_5 is that the scattering angle can become zero, at which point the on-shell Coulomb-scattering cross section is infinite. We evaluated the nuclear part of $d\sigma/d\Omega$ from elastic scattering phase shifts[24] so it was convenient to replace the usual on-shell Coulomb amplitude[25] by the off-shell amplitude[26]

$$f(\vec{k}_i, k, \vec{k}_f) = -\exp[-i\eta \ln(|\vec{k}_i - \vec{k}_f|^2/4k^2)]/(|\vec{k}_i - \vec{k}_f|^2 R), \tag{8}$$

where $\vec{k}_i$ and $\vec{k}_f$ are the relative wave vectors in the initial- and final-state pp system and k is the wave number associated with the channel energy (= average energy in this case). η and R have their usual definition.[21, 25] This amplitude reduces to the on-shell amplitude[25] for $|\vec{k}_i| = k = |\vec{k}_f|$, but it contains no singularities if $\vec{k}_i \neq \vec{k}_f$ and $k \neq 0$ which is the case here (even at $\theta_{\text{msia}} = 0$). The cross section $d\sigma/d\Omega$ in Eq. (7) was evaluated using the Coulomb amplitude of Eq. (8) and the nuclear-bar phase shifts of Ref. 24 evaluated at the average pp c.m. energy.

E. Final-State-Interaction Terms

For small nucleon-nucleon relative energies[27] the Watson-Migdal[18] enhancement factors F_{np} and F_{pp} are exactly those used by Brückman *et al.*[19, 20] in their analysis of the ^{1}H(d, $2p$)n reaction. We did not vary the nucleon-nucleon scattering lengths and effective ranges which are parameters of F_{np} and F_{pp}. These parameters were given the values determined from elastic np and pp scattering at low energies.[28]

F_{np} contains independent contributions from singlet and triplet s-wave np interactions. By careful analysis of the shape of the np-FSI peak in ^{1}H(d, $2p$)n Brückmann *et al*[19] succeeded in separately determining the singlet and triplet contributions to F_{np}. This separation procedure has recently been verified by an exact three-body calculation.[29] We used the singlet/triplet ratio as determined by Brückmann *et al*[19] at the c.m. angle corresponding to $p + d \to p + d^*$ at $\theta_p = 43°$, the angle of our partial Dalitz plot. (d^* refers to the "quasiparticle" composed of a strongly interacting np pair at $E_{np} \approx 0$.) Only the over-all normalizations of F_{np} and F_{pp} were varied in fitting the Dalitz plot data.

Because there are two protons in the final state, F_{np} contributes differently depending on whether proton 3 or proton 4 is the one involved in the np-FSI. The plots labeled np(35) FSI and np(45) FSI in Fig. 6 show the contribution of F_{np} to the Dalitz plot for these two cases.

The plot labeled pp-FSI in Fig. 6 shows the contribution of the F_{pp} term in Eq. (6), and the final plot labeled TOTAL in Fig. 6 shows the sum of the five other plots. The most prominent features in the total Dalitz plot are the large peaks from the pp-QFS term and the np-FSI term involving the neutron with proton 3. The kinematic variables $|\vec{p}_5|$ and E_{35} which most sensitively effect the QFS and np(35)-FSI plots have definite values at each point in the partial Dalitz plot because they do not depend on the angle of emission of proton 3 which was integrated over in forming the plot. Although the spectra at individual angle pairs are strongly peaked at small values of the relative energies E_{45} and E_{34}, this peaking is washed out in the Dalitz plot because each point inside the boundary of the plot corresponds to a range of values for E_{45} and E_{34} depending on the range of kinematically allowed angles for proton 3.

F. Comparison Between Simulation and Data

Figure 5 shows a comparison of the model simulation discussed above with the measured ^{2}H(p, $2p$)n

data. The major features of the measured Dalitz plot are reproduced in the simulation. Some of the apparent differences between the data and the simulation are significant and some are probably due to finite resolution effects which were not included in the simulation. The difference between the simulation and the data in the region of the quasifree-scattering peak (near $E_3 = E_4 = 19$ MeV) is due primarily to finite resolution effects which cause the peak in the data to be smeared out somewhat compared to the simulation. On the other hand, the difference in the region of the np-FSI peak at $E_3 = 6$ MeV, $E_4 = 27$ MeV cannot be accounted for by resolution effects. It may be that an explicit inclusion in the simulation of the angular variation of the np-FSI cross section[19] would partially correct the discrepancy in this region. We believe the most significant difference between the simulation and the data is the minimum in the data around $E_3 = E_4 = 17.5$ MeV, just inside the QFS peak. The minimum does *not* occur in the simulation, which upholds the contention of Ref. 11 that it is due to a destructive interference effect. Interference effects are in no way included in the model discussed in this paper, since this model is an incoherent sum of cross-section terms rather than the sum of amplitudes which would be required to produce interference.

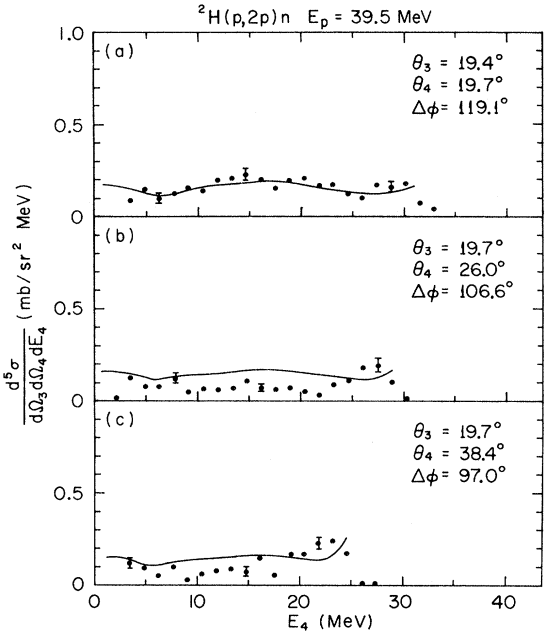

FIG. 7. Spectra of the cross section $d^5\sigma/d\Omega_3 d\Omega_4 dE_4$ at selected pairs of angles chosen to avoid as much as possible the effects of QFS and FSI. The points are the measured data with typical statistical uncertainties indicated by vertical error bars. The solid curves are the predictions of the model discussed in Sec. IV of this article.

G. Comparison of the Model with Individual Spectra

The partial Dalitz plot was chosen as the form of the $^2H(p,2p)n$ data for fitting the model expression because it represents the average behavior of the cross section in a large volume of phase space. However, because of the integration performed over some of the kinematic variables, the comparison of the model expression with the Dalitz plot data is a less sensitive test of the model than a comparison with the individual spectra at fixed pairs of proton-emission angles. For this reason, we chose a small number of representative angle pairs for comparison with the model calculation. In comparing the model expression with the individual spectra, the constants and fitting parameters were not varied from the values determined from fitting the Dalitz plot data.

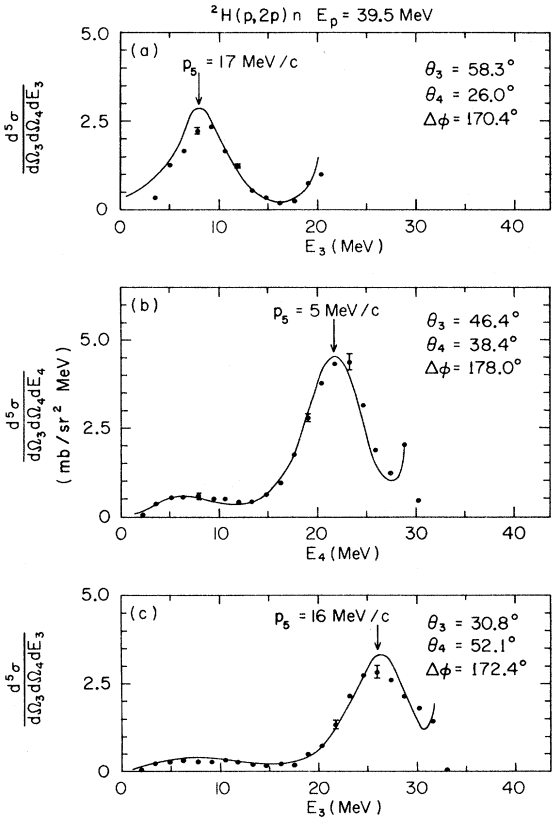

FIG. 8. Spectra of the cross section at pairs of angles chosen to emphasize the effects of pp QFS. Vertical arrows indicate the points of minimum spectator-neutron momentum in each spectrum. The solid curves are the predictions of the model discussed in Sec. IV of this article.

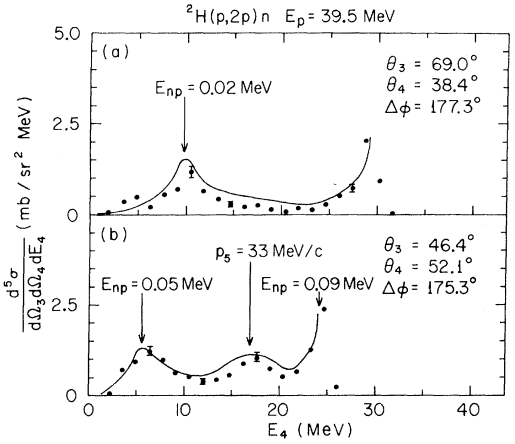

FIG. 9. Spectra of the cross section at pairs of angles chosen to emphasize the effects of *np* FSI. The cross section peaks at small values of the *np* relative energy, as indicated by the arrows. The solid curves are the predictions of the model discussed in Sec. IV of this article.

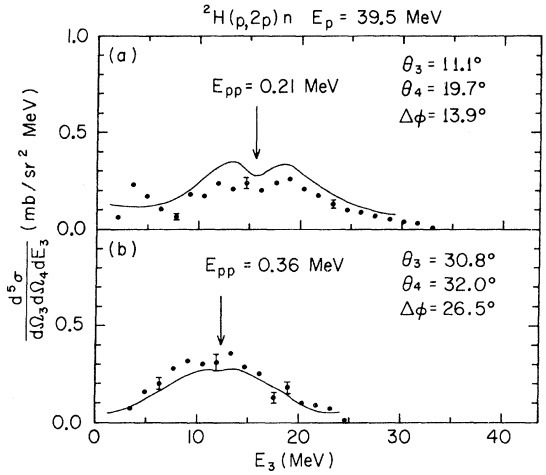

FIG. 10. Spectra chosen to emphasize the effect of *pp* FSI. These spectra and the one in Fig. 4 show a broad peak with a depression in the center caused by the Coulomb repulsion of the two protons. The arrows show the points of minimum *pp* relative energy in each spectrum. The solid curves are the predictions of the model discussed in Sec. IV of this article.

Figure 7 shows three spectra chosen to avoid as much as possible the influences of QFS and FSI processes on the cross section. The solid curves are the predictions of the model expression. The shape of the predicted cross section for these angles is largely determined by a combination of the phase-space and *pp*-FSI terms in Eq. (6).

Figure 8 shows three spectra chosen to emphasize the effects of *pp* QFS. The cross section peaks at the point of minimum momentum transfer to the neutron as indicated by the vertical arrows in each spectrum. There is also a broad peak due to *np* FSI in the two lower spectra of Fig. 8.

Figure 9 shows two spectra chosen to emphasize the effect of the *np* FSI. The spectra exhibit peaks at the points of minimum *np* relative energy, as indicated by the vertical arrows. The lower spectrum also exhibits a peak due to *pp* QFS.

Figures 4 and 10 show three spectra chosen to emphasize the effect of *pp* FSI. The spectra exhibit a broad peak which is split by the Coulomb repulsion of the two protons. The two maximum points of the cross section are at a relative energy of $E_{pp} \approx 0.4$ MeV, on either side of the Coulomb minimum. As the minimum *pp* relative energy increases from spectrum to spectrum in the sequence Fig. 4, Fig. 10(a), Fig. 10(b), the depth of the Coulomb-minimum decreases.

V. SUMMARY AND CONCLUSIONS

We have compared the ^{2}H(p, 2p)n cross section at $E_p = 39.5$ MeV over a large region of phase space with a model which expresses the cross section as an incoherent sum of terms to represent the three major mechanisms, statistical processes, proton-proton quasifree scattering, and nucleon-nucleon final-state interactions. The model reproduces the positions of the peaks observed in the partial Dalitz plot cross section and in the individual angle pairs, but it is quantitatively correct only in the region of phase space dominated by *pp* QFS. The model comparison is entirely consistent with the identification of the minimum in the partial Dalitz plot cross section[11] as being due to destructive interference. The importance of extreme destructive interference effects has also been recently verified in exact separable-potential calculations.[30]

ACKNOWLEDGMENTS

The authors are most grateful to Professor J. A. McIntyre for the great investment he made in directing the design, fabrication, and initial operation of the spherical-chamber system. Dr. D. P. Saylor also greatly deserves our thanks for his contribution to the design and construction of the chamber and for many helpful discussions on the interpretation of the data. We thank Dr. R. F. Schilling, Dr. J. M. Burns, and Dr. P. H. Beatty for assistance in the initial checkout of the system and early data acquisition. We thank E. E. Vezey for his skillful fabrication of the mechanical equipment used in this experiment.

*Work supported by the National Science Foundation.

[1]The use of 4π geometry to study $p-d$ breakup is also reported by B. J. Wielinga, G. J. F. Blommestijn, R. van Dantzig, K. Mulder, A. D. Ijpenberg, I. Slaus, W. M. Kloet, and J. A. Tjon, *Few Particle Problems in the Nuclear Interaction* (North-Holland, Amsterdam, 1972), p. 515.

[2]M. Jain and G. D. Doolen, Phys. Rev. C 8, 124 (1973).

[3]D. P. Saylor, J. A. McIntyre, J. D. Bronson, J. M. Burns, J. G. Rogers, R. F. Schilling, and E. E. Vezey, Nucl. Instrum. Methods 94, 253 (1971).

[4]A DCB is a discriminator-coincidence-buffer unit used to encode the anode signals into binary form.

[5]J. M. Burns, Ph.D. thesis, Texas A&M University, 1970 (unpublished).

[6]L. N. Blumberg, E. E. Gross, A. Van der Woude, A. Zucker, and R. H. Bassel, Phys. Rev. 147, 812 (1966).

[7]R. L. Craun and D. L. Smith, Nucl. Instrum. Methods 80, 239 (1970).

[8]The error quoted is the combined effect of uncertainty in the monitor-detector angle and uncertainty in the measured carbon cross section reported in Ref. 6.

[9]D. J. Margaziotis, G. Paić, J. C. Young, J. W. Verba, W. J. Braithwaite, J. M. Cameron, D. W. Storm, and T. A. Cahill, Phys. Rev. C 2, 2050 (1970); E. L. Petersen, R. G. Allas, R. O. Bondelid, A. G. Pieper, and R. B. Theus, Phys. Lett. 31B, 209 (1970); J. L. Durand, J. Arvieux, A. Fiore, C. Perrin, and M. Durand, Phys. Rev. C 6, 393 (1972).

[10]J. G. Rogers, Bull. Am. Phys. Soc. 16, 512 (1971); A. Niiler, W. von Witsch, G. C. Phillips, C. Joseph, and V. Valković, Phys. Rev. C 1, 1342 (1970).

[11]J. G. Rogers, D. P. Saylor, J. D. Bronson, and M. Jain, Phys. Rev. Lett. 29, 1181 (1972).

[12]C. Møller, Kgl. Danske Videnskab. Selskab, Mat.-Fys. Medd. 23, 1 (1945).

[13]The use of a δ function to explicitly guarentee energy conservation in a model calculation of $d^6\sigma/d\Omega_3 d\Omega_4 dE_3 dE_4$ is reported in G. Jacob and Th. A. J. Maris, Rev. Mod. Phys. 38, 121 (1966). In Eq. (3.23) of this reference, the energy-conserving δ function is included in $d^6\sigma/d\Omega_3 d\Omega_4 dE_3 dE_4$. We have transformed $\delta(E_1+Q-E_3-E_4-E_5)$ to $\delta(\theta_3'-\theta_3)$ and included the resulting Jacobian in our $d^6\sigma/d\Omega_3 d\Omega_4 dE_3 dE_4$.

[14]The coverage coefficient is given by $e_i = 4\pi/96\Delta\Omega_i$ for each of the 96 detectors in the "coarse" system. The solid angle subtended by each detector ($\Delta\Omega_i$) is approximately 2.3 msr.

[15]R. Hagedorn, *Relativistic Kinematics* (Benjamin, New York, 1964), Chap. 7.

[16]M. Jain, Ph.D. thesis, University of Maryland, 1969 (unpublished).

[17]G. Paić, J. C. Young, and D. J. Margaziotis, Phys. Lett. 32B, 437 (1970).

[18]K. M. Watson, Phys. Rev. 88, 1163 (1952); A. B. Migdal, Zh. Eksperim. Teor. Fiz. 28, 3 (1955) [transl.: Soviet Phys. – JETP 1, 2 (1955)].

[19]H. Brückmann, W. Kluge, H. Matthäy, L. Schänzler, and K. Wick, Nucl. Phys. A157, 209 (1970).

[20]H. Brückmann, W. Kluge, H. Matthäy, L. Schänzler, and K. Wick, Phys. Lett. 30B, 460 (1969); H. Brückmann, W. Kluge, H. Matthäy, L. Schänzler, and K. Wick, Institut für Kernphysik–Karlsruhe Report No. 1172, 1970 (unpublished).

[21]M. A. Preston, *Physics of the Nucleus* (Addison-Wesley, Reading, Mass., 1962), p. 32.

[22]Throughout this article we use the convention for the three-body reaction $1+2 \rightarrow 3+4+5$ that particle 1 is the bombarding particle, particle 2 the target particle, particles 3 and 4 are the detected particles, and particle 5 is the undetected particle. E and p are the symbols used to represent an individual particle's kinetic energy and momentum, respectively.

[23]For a discussion of possible prescriptions for evaluating $d\sigma/d\Omega$ see Ref. 16; M. Jain, P. G. Roos, H. G. Pugh, and H. D. Holmgren, Nucl. Phys. A153, 49 (1970); and D. I. Bonbright, Ph.D. thesis, University of Maryland, 1970 (unpublished).

[24]M. H. MacGregor, R. A. Arndt, and R. M. Wright, Phys. Rev. 182, 1714 (1969).

[25]The on-shell Coulomb amplitude as well as the nucleon-nucleon phase-shift formulas are in H. P. Stapp, T. J. Ypsilantis, and N. Metropolis, Phys. Rev. 105, 302 (1957).

[26]J. Nuttall, private communication; M. L. Goldberger and K. M. Watson, *Collision Theory* (Wiley, New York, 1967).

[27]F_{np} and F_{pp} were joined smoothly onto a phase-space function above nucleon-nucleon relative energies of 7.5 MeV because the Watson-Migdal formalism is valid only for "low" relative energies.

[28]W. T. H. van Oers and I. Slaus, Phys. Rev. 160, 853 (1967).

[29]W. Ebenhöh, Nucl. Phys. A191, 97 (1972).

[30]M. Jain, J. G. Rogers, and D. P. Saylor, to be published.